

Biological X-ray diffraction measurements with a novel two-dimensional gaseous pixel detector†

Amir Sarvestani,^{a*} Heinz Amenitsch,^b Sigrid Bernstorff,^b Hans-Jürgen Besch,^a Ralf H. Menk,^b Andre Orthen,^a Nikolaj Pavel,^a Michael Rappolt,^b Norbert Sauer^a and Albert H. Walenta^a

^aFachbereich Physik, Universität-GH Siegen, 57068 Siegen, Germany, and ^bELETTRA, Sincrotrone Trieste, SS 14, km 163.5, Basovizza, 34012 Trieste, Italy.
E-mail: sarvest@alwa02.physik.uni-siegen.de

(Received 15 March 1999; accepted 1 June 1999)

In order to exploit the potential of modern X-ray diffraction studies to its full extent, a new generation of appropriate detectors is required. Here, a small prototype ($28 \times 28 \text{ mm}^2$ active area) of a novel two-dimensional pixel detector is presented which satisfies most of the requirements. It is based on a gaseous single-photon counter with asynchronous readout and interpolating position encoding, combining the advantages of a pure pixel readout (high local and global rate capability) with those of a projecting readout (small number of channels). In order to demonstrate the suitability of this detector for X-ray diffraction applications, measurements at a synchrotron radiation source have been performed recording diffraction patterns from different biological samples (rat tail tendon collagen, phospholipid and protein crystal). These measurements have proven the good spatial resolution, the high intensity precision and the high local rate capability. Moreover, the single-photon readout was utilized in order to perform time-resolved measurements in the case of SAXS studies and to apply fine angular slicing in the case of protein crystallography. The detector has a high reliability and robustness, particularly when compared with conventional gaseous detectors, and the technology used can be easily extended to large active areas.

Keywords: two-dimensional pixel detectors; gas-filled single-photon counters; small-angle X-ray scattering; protein crystallography; time-resolved X-ray imaging.

1. Introduction

The increase of the brilliance of recent synchrotron radiation sources was not accompanied by an adequate increase of the detector performance. In particular, in the case of modern diffraction applications, such as time-resolved small-angle X-ray scattering (SAXS) or protein crystallography, where the requirements in terms of detector performance are exceptionally high, the experiments are often detector-limited (*e.g.* Kriechbaum *et al.*, 1989; Helliwell *et al.*, 1993). Therefore, several research groups around the world are currently concerned with the development of advanced detectors for the aforesaid applications (*e.g.* Stanton *et al.*, 1993; Datte *et al.*, 1997; Lewis *et al.*, 1997; Thoms, 1997; Eikenberry *et al.*, 1998).

X-ray detectors can be grouped into two basic classes: integrating systems (*e.g.* images plates, CCD-based devices) and single-photon counters (*e.g.* gaseous proportional counters, semiconductor pixel detectors).

Integrating detectors are dominant in crystallography due to the generally high rate capability, the good spatial

resolution and the large pixel number. However, the limited dynamic range, the intrinsic noise and the slow readout time often cause tremendous restrictions concerning the data quality (*e.g.* poor high-resolution data, radiation damage on the sample due to long acquisition times). As a result, valuable beam time is often wasted by large dead times or by collecting unusable data.

Single-photon counters are widely used in the case of small-angle X-ray scattering where the high dynamic range, the low noise level and the fast readout allow precise time-resolved measurements. However, the limited number of pixels – most systems are one-dimensional – and the count-rate limitations prevent the exploitation of the source power to its full extent. Consequently, the primary beam often has to be attenuated in order to protect the detector from damage and the diffraction pattern is acquired by time- and dose-consuming scans.

Certainly, a single-photon-counting multipixel detector ensuring a high rate capability would combine the advantages of both detector types. However, the required number of readout channels would go beyond the scope of costs and effort. On the other hand, a single-photon counter with projective readout, such as the RAPID

† Work supported by the European Community (contract No. FMBICT980104 and No. FMBICT961694).

detector which is, in terms of performance, already advanced (Lewis *et al.*, 1997), will always be limited in the global rate capability in spite of sophisticated signal processing (realistically by approximately 10^7 Hz).

The detector which is presented in this paper is a hybrid of a pure pixel detector and a projective system. As described below in detail, the sensitive area is subdivided into quadratic cells which are read out parallel and asynchronously. Through a local interpolation inside such a cell a spatial resolution can be achieved which is much smaller than the cell dimension. Thus, a truly two-dimensional readout enabling very fast data processing is combined with a method to reduce the number of electronic channels by at least two orders of magnitude. Due to the separate readout and storage of each single event, almost any time resolution, even in the sub-microsecond domain, can be achieved.

The measurements performed with the prototype detector, as presented here and in previous publications, have been focused on evaluating the suitability of this instrument for X-ray diffraction studies. This included investigations of the position resolution, the intensity precision, the rate capability and the time resolution, all performed with biological samples using the SAXS beamline at the third-generation synchrotron radiation source ELETTRA.

2. Detector set-up

A detailed description of the detector has already been presented in earlier works (see Besch *et al.*, 1997; Sarvestani *et al.*, 1998a). Here, only the main features are briefly summarized. As depicted in Fig. 1, the photons entering the detector through the entrance window (thin carbon fibre) and the drift cathode (aluminized Mylar foil) are absorbed by the detector gas (typically a xenon/ CO_2 mixture). During this process primary charge is generated. In the constant drift field (24 mm length) the ions are transported

to the drift cathode, while the electrons are transported to the gas gain structure (MicroCAT; see Sarvestani *et al.*, 1998a). The MicroCAT (supplied by Koenen Siebdrucktechnik, 85521 Ottobrunn, Germany) consists of a 55 μm -thick nickel foil perforated with microholes (116 μm diameter) in a hexagonal arrangement with a pitch of 164 μm . At a distance of 225 μm below the MicroCAT, which is supplied with negative high voltage (typically -1000 V), the grounded anode is placed. Due to this configuration the electric field strongly increases in the vicinity of the microholes, reaching an almost constant plateau between the MicroCAT and the anode (typically $40\text{--}80$ kV cm^{-1}). Therefore, the gas amplification arising at such high fields is distributed along a relatively long path (in comparison with wire or microstrip chambers where the gas gain is localized typically along a 20 μm path).

The anode serves also as the position-encoding structure. It consists of specially structured resistive layers printed on a ceramic substrate which also contains a quadratic grid of readout nodes with 4 mm pitch being through-connected to pads on the back (see Besch *et al.*, 1997). Each node is separately connected to an amplifier followed by an FADC. A square of four readout nodes defines an interpolation cell (4×4 mm² in size). Each cell consists of a high-resistive central area (100 $\text{k}\Omega$ square⁻¹) surrounded by a low-resistive border (1 $\text{k}\Omega$ square⁻¹) (see detail in Fig. 1). This design forces the charge, which is deposited in such a cell, to flow to the low resistive borders where a charge division to the adjacent readout nodes occurs. Hence, from the signal distribution on the four nodes surrounding the cell, the position of the event can be calculated by simple linear equations (similar to the position interpolation method in the case of one-dimensional resistive charge division). Currently, this system allows a 20×20 pixel interpolation per readout node, reducing the number of channels by a factor of 400 compared with a pure pixel detector. In total, the prototype detector has 8×8 readout nodes fully

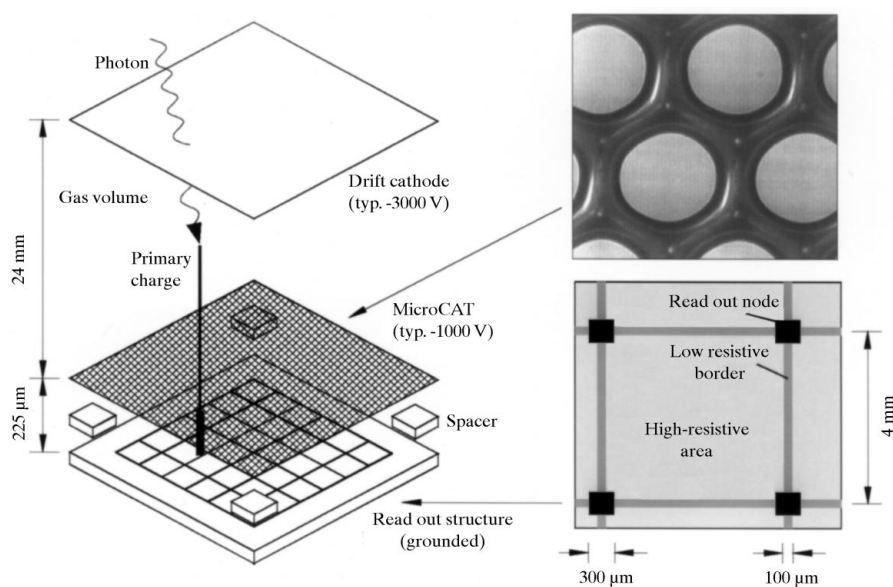


Figure 1
Schematic set-up of the two-dimensional detector (the active area is 28×28 mm²).

equipped with electronics, thus 7×7 interpolations cells. This corresponds to an active area of $28 \times 28 \text{ mm}^2$ and effectively 140×140 pixels with a pixel size of $200 \times 200 \mu\text{m}^2$.

All electronics used for readout are in-house developments based on hybrid and multilayer technology. The 64 charge-sensitive low-resistive input amplifiers conjunct pre-amplification and shaping on one module. The amplifiers are followed by 64 analogue-to-digital converters (flash ADCs) distributed among four boards. They are operated as transient recorders sampling at a rate of 8 MHz with 8 bit resolution and 16 samples per signal. The system is triggered by the signals from the MicroCAT structure (global trigger), *i.e.* all 64 channels are read out in parallel. The sampled data are latched in 64 buffer RAMs (each 1 kByte memory). Once the RAMs are full the readout cycle starts, in which data are transferred *via* a standard 32 bit PCI I/O interface into a PC. This part is currently the bottleneck of the readout electronics reducing the effective readout speed to some kHz. Nevertheless, still very high time resolutions can be obtained, since the writing cycle is almost dead-time free and all signals can be stored together with the detection time. Signal calibration, position interpolation and image formation is performed on-line by software on the PC.

3. General performance

Measurements evaluating the general performance of this detector have already been reported (see Besch *et al.*, 1997; Sarvestani *et al.*, 1998a; Sarvestani, Besch, Menk *et al.*, 1998).

The MicroCAT, which is responsible for the gas amplification, provides a stable operation at gas gains exceeding values of 10^4 depending on gas mixture, gas pressure, spacer gap and geometry of the MicroCAT (three different types are available). When taking into consideration the 300–1000 primary electrons typically being produced by 6–24 keV photons in standard gas mixtures, the achievable gas gain yields a sufficiently large signal-to-noise ratio for the resistive interpolation method chosen here. As experimentally observed, the gas gain is very sensitive to local variations of the spacer gap. Therefore, in a set-up without any spacers within the active area the structure has to be stretched and aligned sufficiently to keep the variations at a minimum (this is performed with the prototype detector presented here). However, for larger active areas the use of intrinsic spacers within the active area is unavoidable. In this connection a chamber has recently been equipped with a new spacer system which ensures a constant distance between cathode and anode even for very large active areas (set-up and measurements will be published soon).

Detailed experimental studies have proven the exceptionally high rate capability of this detector compared with conventional gas detectors (*e.g.* wire or microstrip chambers). First, no drop of the gas gain has been observed even

for values as high as 7 MHz mm^{-2} (at a gas gain of 3000 and a photon energy of 8 keV). Second, space charge effects are suppressed by the very low ion feedback (*i.e.* fraction of ions produced in the avalanche which drift back through the holes of the MicroCAT into the drift region). It was demonstrated that, even for the extreme case of a hot spot of 1 MHz count rate neighboured by a weak spot at a distance of $500 \mu\text{m}$, no significant spatial distortions occur (owing to the current rate limitation of the digital readout electronics to a few kHz, this measurement was performed

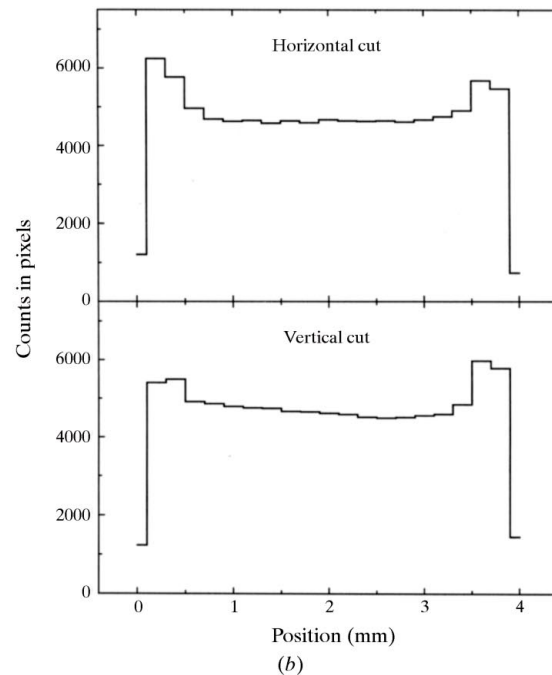
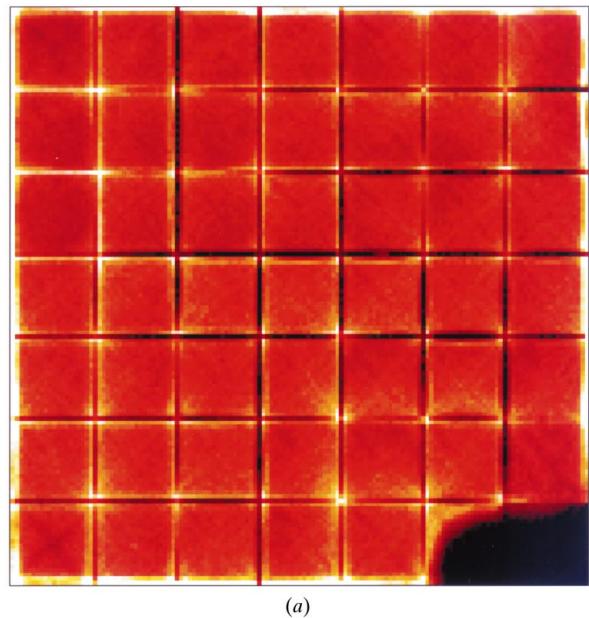


Figure 2

Detector response from a flat-field illumination: (a) image of the entire active area of $28 \times 28 \text{ mm}^2$ (at the bottom right two channels are defect); (b) profile cuts across the centre of a single cell (averaged over the inner 5×5 cells).

with a poor lifetime). Eventually, dead-time effects due to signal pile-up can be kept at a low level up to a rate of 1 MHz when using fast shaping amplifiers. Obviously, simultaneous events within one interpolation cell cannot be processed. However, the fast signal generation (values down to 100 ns are feasible) allows a few 1 MHz spots within a single cell to be processed, which is sufficient for most diffraction applications. At gas gain values well above the level required for imaging operation, rate-dependent breakdowns were observed. However, these breakdowns do not induce any damage to the detector or the electronics underlining the high robustness of this system.

The energy resolution of the detector is around 20% FWHM (for 5.9 keV energy and 10^5 Pa argon-based gas mixture) deteriorating slightly with pressure. Due to the inverse scaling of the energy resolution with the square root of the energy it becomes better for higher energies. In the case of monochromatic diffraction applications the energy resolution is solely required to ensure a sufficient separation between photon signals and noise which is obviously possible with the resolution values obtained.

Due to the negligible dark rate, the intensity precision obtained is only limited by Poisson statistics, as expected for a single-photon counting detector.

By choosing adapted gas mixtures, gas pressures and drift lengths one can ensure a sufficient quantum efficiency for the required X-ray energy range. In the case of energies below 12 keV and xenon-based gas mixtures at atmospheric pressure, a quantum efficiency larger than 70% is obtained for a 24 mm drift length. When choosing energies up to 24 keV the detector has to be operated with xenon-based

gas mixtures at pressures up to 6×10^5 Pa in order to obtain the aforesaid quantum efficiency for 24 mm drift length. So far, the detector has been successfully operated with different argon-, krypton- and xenon-based gas mixtures at atmospheric pressures. Using argon-based gas mixtures, high-pressure operation up to 6×10^5 Pa was performed.

4. Imaging performance

All images presented in this paper have been obtained by applying simple linear interpolation formulae in order to calculate the position of the event from the four nodes of the cell which is hit (for details of the encoding algorithms, see Besch *et al.*, 1997; Sarvestani *et al.*, 1998b).

4.1. Uniformity

Fig. 2 shows the detector response being uniformly illuminated with a ^{55}Fe source (5.9 keV) placed 20 cm in front of the entrance window (the resulting rate was 4 kHz). The detector was operated with an Ar/Xe/CO₂ (40/40/20) mixture at 1.2×10^5 Pa, a gas gain of about 4000 (yielding approximately 10^6 electrons per photon), and a drift field of 750 V cm^{-1} . At the borderlines between the interpolation cells significant distortions occur, since those regions are very sensitive to inaccuracies in signal determination, *i.e.* resistive noise, electronic noise and cross-talk. The relatively low resistive borders (the node-to-node resistance is $\sim 20 \text{ k}\Omega$) of the given readout structure yield already a resistive noise of the order of 6000 electrons r.m.s. Moreover, a significant cross-talk between neighboured channels

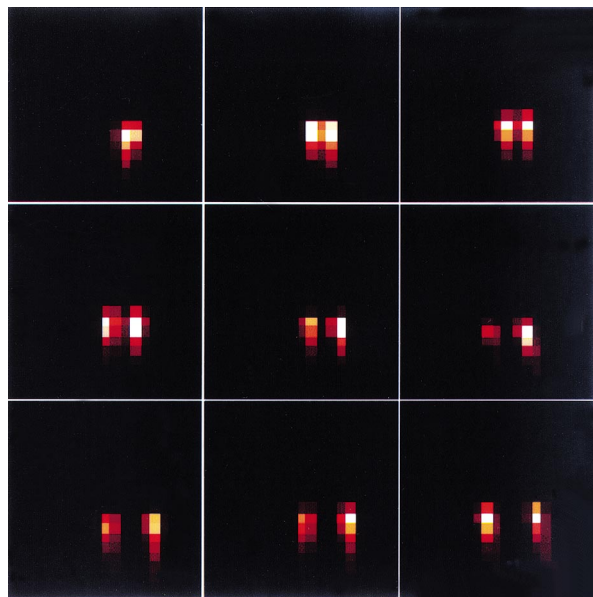


Figure 3
Recorded image ($12 \times 12 \text{ mm}^2$ detail) from a collimator with nine double holes with different distances: 200, 300, 400, 500, 600, 700, 800, 900, 1000 μm (starting from top left moving horizontally); the thin white lines indicate the borders of the interpolation cells ($4 \times 4 \text{ mm}^2$ cell size).



Figure 4
Recorded image ($20 \times 20 \text{ mm}^2$ detail) of a 'SAXS'-shaped collimator; the spots in the lower part of the image arise from five holes attenuated with aluminium foils with different thicknesses; the thin white lines indicate the borders of the interpolation cells ($4 \times 4 \text{ mm}^2$ cell size).

of up to 7% occurs. Both effects are dominant for the distortions at the cell borders. In the future the resistive noise will be reduced by adapting the resistances of the readout structure, and cross-talk will be suppressed by a modification of the readout electronics. It is expected that this will enhance distinctly the image uniformity. Besides, it has already been demonstrated that the use of non-linear interpolation algorithms will suppress spatial distortions at the cell borders (Sarvestani *et al.*, 1998b).

4.2. Spatial resolution

In order to evaluate the spatial resolution of the detector, specially designed collimators have been utilized. The measurements have been performed at the SAXS beamline at ELETTRA, Sincrotrone Trieste, Italy (Amenitsch *et al.*, 1998; Bernstorff *et al.*, 1998). By using a diffuse scattering target (a pure iron foil), illuminated with the 8 keV primary beam, a flat-field illumination was obtained. The detector was placed at a distance of 77 cm from the target.

Fig. 3 shows a recorded image when placing a collimator with double holes with different distances between 200 and 1000 μm directly in front of the detector. Each hole has a diameter of about 150 μm . Two spots can clearly be resolved down to a hole distance of 300 μm . Slight parallax distortions in the vertical direction are observed, because the detector was mounted on a translation device moving on a plane surface perpendicular to the beam direction, so that photons were entering the detector at angles different from normal incidence. The spatial resolution cannot be determined consistently for all regions since the influence of the spatial distortions varies along the active area. Due to the absence of distortions the best results are obtained in the cell centre, where values around 300 μm FWHM are typical. By reducing the cell size, smaller resolution values can be achieved. For instance, in the case of the readout structure used in the first place, consisting of $2 \times 2 \text{ mm}^2$ cells, a spatial resolution of less than 200 μm FWHM was obtained.

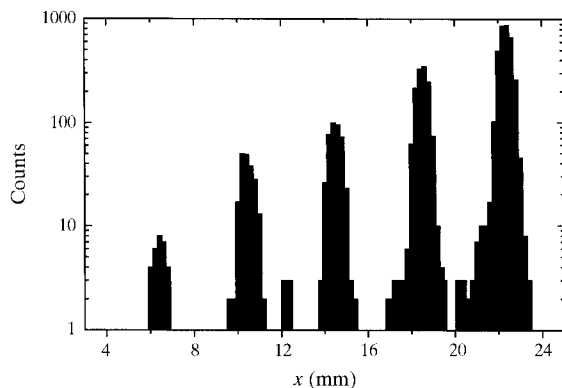


Figure 5

Projected profile across the spots from the lower part of the image shown in Fig. 4. The counts in the direction perpendicular to the profile were integrated over a radius of 1 mm with respect to the central line crossing the spots.

The image of a special contour collimator, as shown in Fig. 4, also verifies the correct image reproduction, apart from the distortions at the cell borders which were discussed above. The spots in the lower part of the image arise from five holes which are placed in a row with a pitch of 4 mm and a diameter of 1 mm. The holes were attenuated with (starting from the left) 4, 3, 2, 1 and no aluminium foils, each with a thickness of 25 μm . The extracted profile shown in Fig. 5 verifies linear operation. As expected, an exponential dependence is observed which is within the systematic errors (due to variations in the hole diameters, different foil thicknesses, non-uniformity of the illumination *etc.*).

4.3. Drift field adjustment and gain calibration

In order to align the drift field, the voltages of the relevant electrodes have been adjusted while monitoring the detector image from a hole grid collimator placed directly in front of the detector and being illuminated uniformly (see §4.2). Due to the large source distance of 77 cm the parallax effect is negligible. Each hole has a diameter of 1 mm and the pitch is 4 mm. The collimator is aligned in such a way that the holes match with the position of the readout nodes at the cell corners. This enables the parallelism of the correctly adjusted drift field to be verified (see Fig. 6).

The hole grid collimator was also utilized to calibrate the gain factors of the different readout channels. Both local gas gain variations and variations in the gain factors of the various electronic components have to be corrected by a software look-up table (these variations can reach values up to a factor of two). Unlike in the case of a uniform illumination, where the pulse height spectrum of each

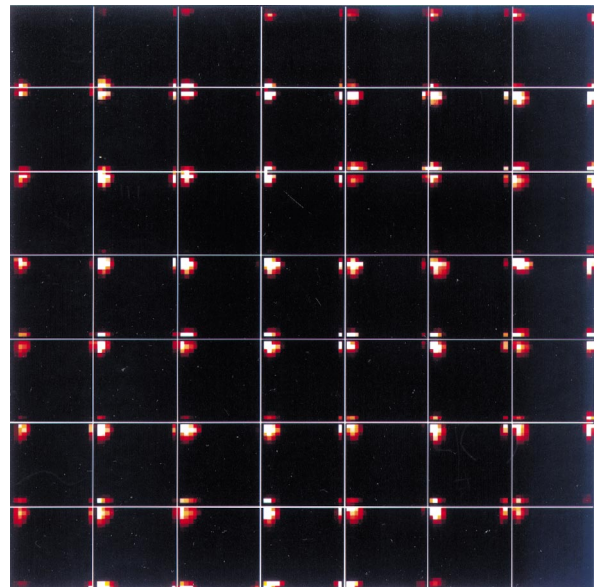


Figure 6

Recorded image (full $28 \times 28 \text{ mm}^2$ active area) from a hole grid collimator (4 mm pitch); this image is used for drift field adjustment and gain calibration.

single node corresponds to a monotonously dropping function, the direct collimation on the nodes yields – in the case of monochromatic radiation – a single-line spectrum (of course convoluted with the energy resolution). For each readout node the amplitude spectrum was extracted and the position of the line within this spectrum (the gain factor) was determined. The gain factors were then used to normalize all node signals resulting in a uniform response of all channels after the gain correction.

4.4. Parallax

Parallax occurs in gaseous detectors with planar geometry when photons enter the conversion medium at an angle different from normal incident (*e.g.* Lewis, 1994). In this case the path of the incoming photons is projected onto the detector plane involving smeared and, occasionally, overlapping spots. It has already been demonstrated by detailed simulation studies as well as by measurements that parallax smearing can be sufficiently reduced by selecting appropriate gas mixtures, gas pressures and sample-to-detector distances (Sarvestani, Walenta *et al.*, 1998; Sarvestani, 1998). According to the results of the simulation studies of protein crystallography experiments using wavelengths of 0.5–1.0 Å and samples with unit cells around 1000 Å, the choice of a xenon-based gas mixture operated at pressures between 1×10^5 and 1×10^6 Pa and a sample-to-detector distance around 1 m suppresses parallax sufficiently. Obviously, these conditions are fulfilled also in small-angle scattering experiments where usually lower energies and smaller diffraction angles are selected.

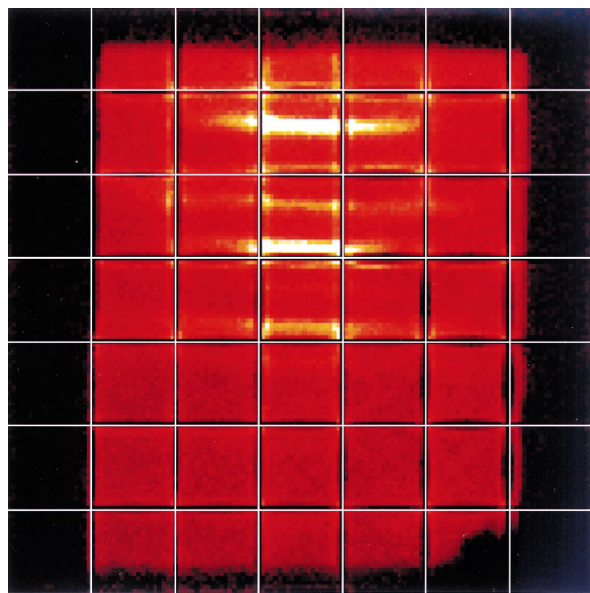


Figure 7

Recorded diffraction pattern from a dry rat tail tendon collagen sample (full $28 \times 28 \text{ mm}^2$ active area); the outer cells were blinded out by a collimator; the thin white lines indicate the cell borders; the average photon number per pixel is about 100.

5. Diffraction measurements

All measurements presented in this chapter have been performed at the SAXS beamline at the Sincrotrone Trieste (Italy) using a monochromatic primary beam of 8 keV and a camera length of 77 cm. The monochromator and the slit systems have been adjusted to achieve the optimum small-angle scattering quality in the vertical direction, yielding an almost rectangular beam profile with a vertical and horizontal expansion of about 0.3 and 1.0 mm, respectively. Details of the characteristics of the beamline and the monochromator are given by Amenitsch *et al.* (1998) and Bernstorff *et al.* (1998), respectively. In order to adjust the photon flux and to protect the detector from extensive flux, different stacks of aluminium foils were used for attenuating the primary beam directly in front of the sample. The detector was operated with a xenon/CO₂ (87/13) mixture at a pressure of $\sim 1.2 \times 10^5$ Pa. During all measurements a gas gain of about 5000 and a drift field of 1000 V cm^{-1} was maintained. Since the images were calculated with simple linear equations, cell border distortions occur in all patterns.

5.1. Rat tail tendon collagen

The first sample, several fibres of dry rat tail tendon collagen, was selected since it is a widely used standard calibration sample for small-angle scattering studies, thus enabling comparisons of the results obtained with this detector with those of other detectors.

From the measured two-dimensional diffraction pattern, as shown in Fig. 7, the different orders of diffraction can be identified. Due to the alignment of the beam stop the pattern starts at the fifth order. The two-dimensional shape of the diffraction structure is clearly visible. However, since several peaks are overlapped by the cell border distortions,

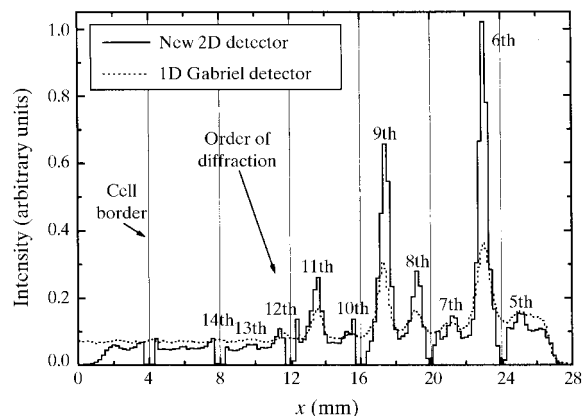


Figure 8

Vertical profile through the dry rat tail tendon collagen diffraction pattern recorded with the two-dimensional detector (for the horizontal direction four pixels, corresponding to $800 \mu\text{m}$, have been summed). For comparison a profile is plotted which has been recorded with a one-dimensional delay line detector (Gabriel type). Both curves are scaled to the same integral. The maximum of the 6th order of the profile from the two-dimensional detector contains 20428 photons, while that of the one-dimensional detector profile contains 27742 photons.

the diffraction structures seem straight rather than arced, as expected. Even in the case of imaging diffraction patterns with an axial symmetry, the two-dimensional detection improves the counting statistics with respect to a one-dimensional detector, and avoids warped diffraction

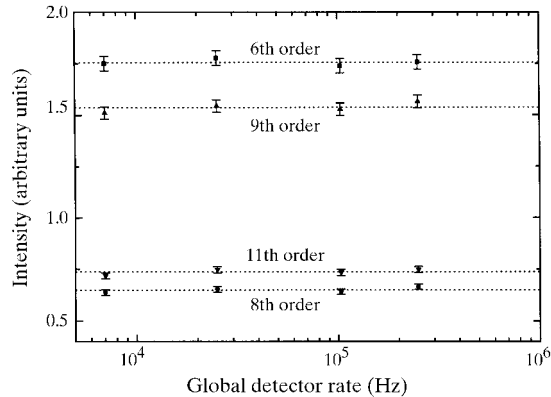


Figure 9
Intensity linearity of the dry rat tail tendon collagen profile as a function of the global rate (over 480 mm^2); the plot shows the intensity of some selected diffraction orders from normalized profiles measured at different photon fluxes.

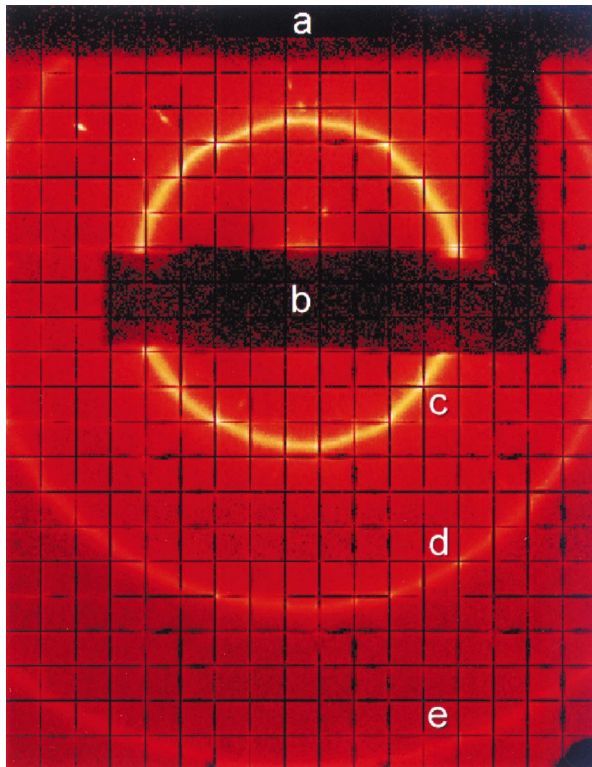


Figure 10
Recorded diffraction pattern (logarithmic scale) from a DSPC lipid sample; the pattern which corresponds to an area of $68 \times 88 \text{ mm}^2$ (340×440 pixel) was acquired by composing 3×4 images which have been recorded separately; (a) shadow of the vacuum vessel, (b) shadow of the beam stop, (c) first-order diffraction ring, (d) second-order diffraction ring, and (e) third-order diffraction ring.

profiles arising in the case of a misaligned one-dimensional detector.

The vertical diffraction profile, shown in Fig. 8, was extracted by applying an adapted cut through the centre of gravity of the two-dimensional diffraction pattern. Owing to the cell border distortions (see §4.1), sharp drops occur every 4 mm in the profile. Diffraction peaks up to the 14th order are clearly visible. For comparison, Fig. 8 shows a diffraction profile from the same sample but recorded with a one-dimensional delay-line detector (Gabriel, 1977). This measurement was performed without changing the sample and the adjustment of the beamline. Nevertheless, distinct differences between the two profiles are visible. The profile from the one-dimensional detector has broader peaks, slightly different intensity ratios of the peaks, and a poorer signal-to-background ratio, even though both measurements have almost the same statistics. Reasonable explanations for this effect are misalignment of the one-dimensional detector with respect to the centre of gravity of the vertically prolonged diffraction profile (*e.g.* parallel offset) and space charge effects impairing the intensity linearity. Moreover, the one-dimensional detector, which was filled with an argon-based gas mixture at a pressure of $\sim 4 \times 10^5 \text{ Pa}$, suffers from parallax smearing, as proven by the slightly asymmetric, thus broadened, peaks.

Single-photon counters suffer often from saturation effects in the case of high rates resulting in non-linearities of the recorded intensity. In order to verify the intensity linearity of the two-dimensional detector, the same profile has been recorded with different incident photon fluxes using aluminium foils to attenuate the primary beam. Fig. 9 shows the relative intensity of some selected diffraction peaks from profiles recorded at different rates, demonstrating the linearity of the measured intensity up to a rate of 250 kHz over the active detector area (this was the maximum rate which could be obtained without changing the beamline optics). In comparison, the one-dimensional delay-line detector starts saturating at rates of $\sim 50 \text{ kHz}$.

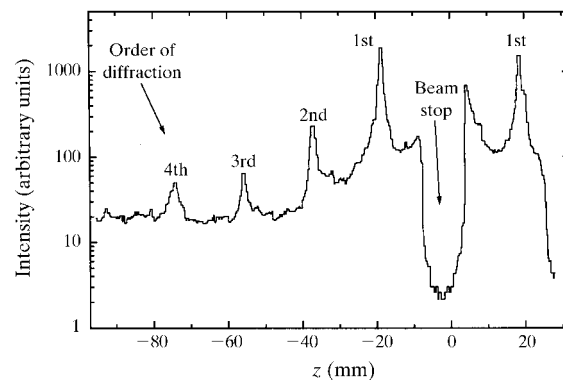


Figure 11
Vertical profile through the diffraction pattern of the DSPC lipid sample; for composing the profile out of six separate patterns the overlap regions were used for scaling the intensity; horizontally 11 pixels (1.2 mm) have been summed; the maximum of the first-order peak corresponds to about 5000 photons.

5.2. DSPC lipid

The second sample, a DSPC lipid (1,2-distearoyl-sn-glycero-3-phosphatidylcholin), features a very strong diffraction power. Fig. 10 shows a pattern which – owing to the limited detector area – has been composed out of 3×4 single images (the images were scaled with respect to each other by using the overlapping border regions). Besides the shadows from the vacuum vessel and the beam stop, the concentric diffraction rings up to the third order are clearly visible. Sporadically, some sharp spots appear in the pattern. Since these spots disappeared completely when the aluminium foils (used for attenuating the primary beam) were removed, they are most likely caused by impurities of the foils.

In a second measurement a vertically prolonged image of the diffraction pattern was recorded ($28 \times 128 \text{ mm}^2$ area), again by composing separate images (six in total). In this

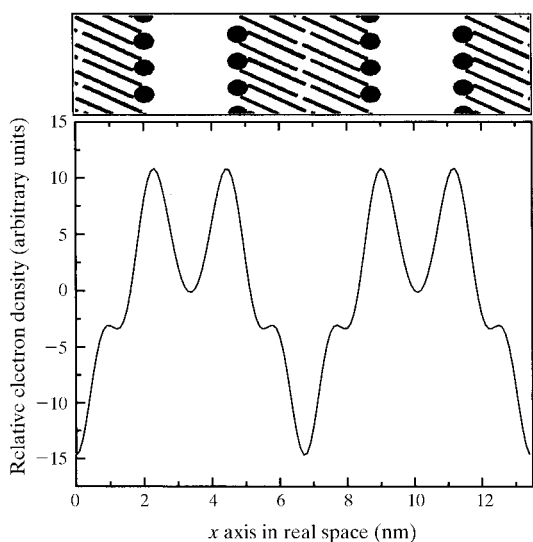


Figure 12

Electron density of the DSPC lipid sample reconstructed from the profile shown in Fig. 11 (using phase information from the literature; see Luzzati *et al.*, 1972); the drawing above the plot shows schematically the structure of the lipid bilayer (the full lines indicate each a fatty acid chain, while the circles indicate the head group region).

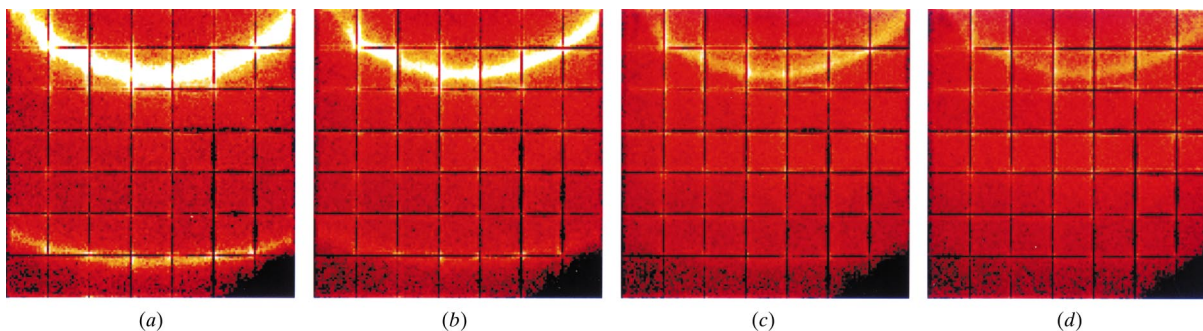


Figure 13

The effect of radiation damage on the diffraction pattern of the DSPC lipid sample; the images ($28 \times 28 \text{ mm}^2$ each, logarithmic scale) show the patterns after a certain illumination time of the sample: (a) 214 s, (b) 1418 s, (c) 3133 s and (d) 4973 s.

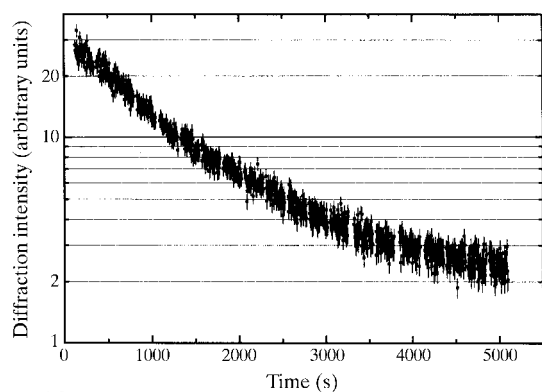
case even the fourth-order diffraction ring was visible, which allowed the vertical diffraction profile shown in Fig. 11 (in the horizontal direction 11 pixels have been averaged) to be extracted. A median filter with a radius of seven pixels was used in order to suppress the sharp cell border distortions but to keep the smoother diffraction profile unchanged (this non-linear filter is applied for a better visualization only, and is not suitable for accurate intensity calculations).

From the profile in Fig. 11 the electron density shown in Fig. 12 was calculated, using *a priori* knowledge about the corresponding phases. The result is in good accordance with electron densities determined from measurements with other detectors (*e.g.* Luzzati *et al.*, 1972; Pressl *et al.*, 1997).

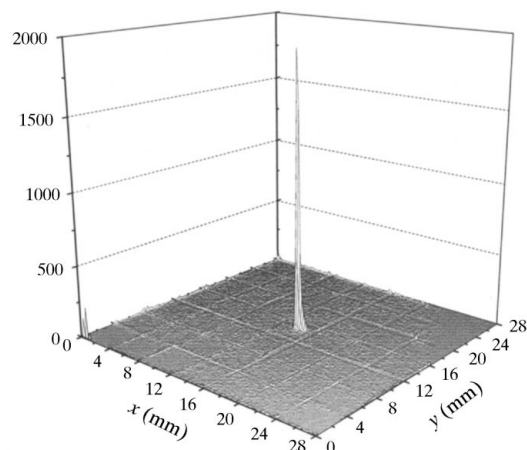
The good time resolution of the detector was utilized in order to monitor the effect of radiation damage on the diffraction pattern. For this purpose the sample has continuously been illuminated with the full primary beam (about $5 \times 10^{11} \text{ photons mm}^{-2} \text{ s}^{-1}$) while the diffraction pattern was recorded with the detector. In principle, a time resolution in the sub-microsecond range is obtainable with the detector, since each photon can be stored together with its detection time (only limited by the rising time of the analogue signal). However, a time slicing of 4.3 s was sufficient since the entire process under investigation lasted about 83 min. The selected patterns in Fig. 13 show the drop of the diffraction intensity, thus the degradation of the lipid structure by radiation damage. The curve shown in Fig. 14 reflects this even more distinctly. Here, the intensity of a fixed portion of the first diffraction order normalized on a selected part of the background (not being overlapped by the diffraction structure) is plotted as a function of the illumination duration. This curve allows quantitative predictions about the degradation process induced by radiation damage.

5.3. Protein crystal

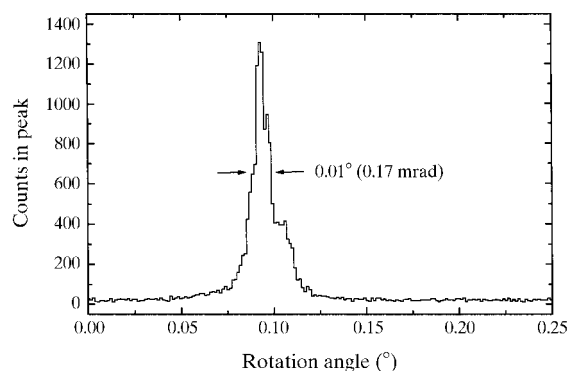
A medium-size protein crystal (unit cell: $a = 53.3$, $b = 72.5$, $c = 72.8 \text{ \AA}$; space group: $P2_12_12_1$) was selected to evaluate the performance of the detector for protein crystallography experiments. The recorded oscillation pattern

**Figure 14**

Intensity of a part of the first-order diffraction ring (normalized on a background section not being overlapped by the diffraction structure) as a function of the illumination duration; the data have been derived from cutting the continuously recorded patterns in time slices of 4.3 s width; the error bars reflect the Poisson fluctuations.

**Figure 15**

Diffraction spot from a protein crystal recorded during a sample rotation of 0.012° ; the spot corresponds to a Bragg angle of $2\theta = 2.2^\circ$, thus a resolution of 41.4 \AA (in consideration of 8 keV beam energy), and is located close to the vertical layer (the rotation axis is located in the horizontal layer).

**Figure 16**

Rocking curve of the diffraction spot shown in Fig. 15; the data have been derived from cutting the continuously recorded pattern in angular slices of 0.001° width; the intensity is determined by summing all entries inside a square area covering the spot and by normalizing it on the surrounding background which is rotation independent.

(0.012° rotation interval), shown in Fig. 15, contains a strong diffraction spot which corresponds to a resolution of 41.4 \AA . One-dimensional profile cuts yield a FWHM of the spot of about $300 \mu\text{m}$, for both the x and the y coordinate. The measurement was performed with a sample rotation at a constant angular speed. Hence, by cutting the data into images with equidistant time slices, as described in the previous section, equidistant angular slices were obtained. An angular width of 0.001° was selected which was also the precision of the stepper motor used for the rotation. From these data the rocking curve (*i.e.* the spot intensity as a function of the sample rotation angle) was derived featuring a FWHM as low as 0.01° (see Fig. 16). It has already been demonstrated elsewhere that the small angular slicing ability of a single-photon counter can tremendously enhance the intensity precision of diffraction spots, thus the quality of the reconstructed object (*e.g.* Kabsch, 1993). The detector used here allows a free choice of any angular slicing adapted to the requirements of the experiment.

6. Conclusions

The measurements which have been performed have demonstrated the suitability of this detector for modern X-ray diffraction applications using synchrotron radiation. High intensity precision, good spatial resolution, high local count-rate capability [as demonstrated by Sarvestani, Besch, Menk *et al.* (1998)], very high time resolution [as demonstrated by Sarvestani *et al.* (1999)] and high robustness are met simultaneously. It is expected that, by suppressing the systematic errors affecting the position encoding, an image uniformity without spatial distortions will be obtained.

After the prototype phase is now completed we are facing the construction of the final large area detector. According to a feasibility study for the extension of the active area to values up to $1 \times 1 \text{ m}^2$, which would be ideal for protein crystallography, no major problems are to be expected (Sarvestani, 1998). However, regarding the readout electronics, a highly integrated multichannel system (at maximum 10000 channels for a $1 \times 1 \text{ m}^2$ detector) still has to be developed. In this regard a first prototype based on an existing VLSI is currently being designed.

The employment of the final detector in X-ray diffraction studies would enhance data quality and shorten acquisition times distinctly. This would allow complex structures to be studied and highly time-resolved *in vivo* experiments to be performed.

References

Amenitsch, H., Rappolt, M., Kirchbaum, M., Mio, H., Laggner, P. & Bernstorff, S. (1998). *J. Synchrotron Rad.* **5**, 506–508.

- Bernstorff, S., Amenitsch, H. & Laggner, P. (1998). *J. Synchrotron Rad.* **5**, 1215–1221.
- Besch, H. J., Junk, M., Meißner, W., Sarvestani, A., Stiehler, R. & Walenta, A. H. (1997). *Nucl. Instrum. Methods*, **A392**, 244–248.
- Datte, P., Beuville, E., Beche, J.-F., Cork, C., Earnest, T., Millaud, J., Nygren, D., Padmore, H., Turko, B. & Xuong, N.-H. (1997). *Nucl. Instrum. Methods*, **A391**, 471–480.
- Eikenberry, E. F., Barna, S. L., Tate, M. W., Rossi, G., Wixted, R. L., Sellin, P. J. & Gruner, S. M. (1998). *J. Synchrotron Rad.* **5**, 252–253.
- Gabriel, A. (1977). *Rev. Sci. Instrum.* **48**, 1303–1305.
- Helliwell, J. R., Ealick, S., Doing, P., Irving, T. & Szebenyi, M. (1993). *Acta Cryst.* **D49**, 120–128.
- Kabsch, W. (1993). *J. Appl. Cryst.* **26**, 795–800.
- Kriechbaum, M., Rapp, G., Hendrix, J. & Laggner, P. (1989). *Rev. Sci. Instrum.* **60**, 2541–2544.
- Lewis, R. A. (1994). *J. Synchrotron Rad.* **1**, 43–53.
- Lewis, R. A., Helsby, W. I., Jones, A. O., Hall, C. J., Parker, B., Sheldon, J., Clifford, P., Hillen, M., Sumner, I., Fore, N. S., Jones, R. W. M. & Roberts, K. M. (1997). *Nucl. Instrum. Methods*, **A392**, 32–41.
- Luzzati, V., Tardieu, A. & Taupin, D. (1972). *J. Mol. Biol.* **64**, 269–286.
- Pressl, K., Jørgensen, K. & Laggner, P. (1997). *Biochem. Biophys. Acta*, **1325**, 1–7.
- Sarvestani, A. (1998). PhD thesis, University of Siegen, Germany.
- Sarvestani, A., Besch, H. J., Junk, M., Meißner, W., Sauer, N., Stiehler, R., Walenta, A. H. & Menk, R. H. (1998a). *Nucl. Instrum. Methods*, **A410**, 238–258.
- Sarvestani, A., Besch, H. J., Junk, M., Meißner, W., Sauer, N., Stiehler, R., Walenta, A. H. & Menk, R. H. (1998b). *Nucl. Instrum. Methods*, **A419**, 444–451.
- Sarvestani, A., Besch, H. J., Menk, R. H., Pavel, N., Sauer, N., Strietzel, C. & Walenta, A. H. (1998). *Nucl. Instrum. Methods B*. Submitted.
- Sarvestani, A., Besch, H. J., Menk, R. H., Pavel, N. A., Sauer, N., Strietzel, C. & Walenta, A. H. (1999). In preparation.
- Sarvestani, A., Walenta, A. H., Busetto, E., Lausi, A. & Fourme, R. (1998). *J. Appl. Cryst.* **31**, 899–909.
- Stanton, M., Phillips, W. C., O'Mara, D., Naday, I. & Westbrook, E. (1993). *Nucl. Instrum. Methods*, **A325**, 558–567.
- Thoms, M. (1997). *Nucl. Instrum. Methods*, **A389**, 437–440.